

# **Parsimonious Modeling of Skeletal Muscle Perfusion: Connecting the Stretched Exponential and Fractional Fickian Diffusion**

David A. Reiter<sup>1,2</sup>, Fatemeh Adelnia<sup>3</sup>, Donnie Cameron<sup>4,5</sup>, Richard G.  
Spencer<sup>6</sup>, Luigi Ferrucci<sup>6</sup>

<sup>1</sup> Department of Radiology & Imaging Sciences

<sup>2</sup> Department of Orthopedics  
Emory University  
Atlanta, GA, USA

<sup>3</sup> Vanderbilt University Institute of Imaging Sciences  
Vanderbilt University, Medical center  
Nashville, TN, USA

<sup>4</sup> Norwich Medical School  
University of East Anglia  
Norwich, UK

<sup>5</sup> C.J. Gorter Center for High Field MRI  
Department of Radiology, Leiden Medical Center  
Leiden, NL

<sup>6</sup> National Institute on Aging  
National Institutes of Health  
Baltimore, MD, USA

Corresponding Author:  
David A. Reiter, Ph.D.  
1841 Clifton Rd.  
Atlanta, GA, 30307  
Email: [dareite@emory.edu](mailto:dareite@emory.edu)

Short title: Fractional Fickian Diffusion Modeling of Skeletal Muscle Perfusion

Word count: 4,958

# Abstract

## Purpose

To develop an anomalous (non-Gaussian) diffusion model for characterizing skeletal muscle perfusion using multi- $b$ -value DWI.

## Theory and Methods

Fick's first law was extended for describing tissue perfusion as anomalous super-diffusion, which is non-Gaussian diffusion exhibiting greater particle spread than that of the Gaussian case. This was accomplished using a space-fractional derivative which gives rise to a power-law relationship between mean squared displacement and time, and produces a stretched exponential signal decay as a function of  $b$ -value. Numerical simulations were used to estimate parameter errors under in vivo conditions, and examine the effect of limited signal-to-noise and residual fat signal. Stretched exponential DWI parameters,  $\alpha$  and  $\mathcal{D}$ , were measured in thigh muscles of four healthy volunteers at rest and following in-magnet exercise. These parameters were related to a stable distribution of jump length probabilities and used to estimate microvascular volume fractions (MVF).

## Results

Numerical simulations showed low dispersion in parameter estimates within 1.5% and 1%, and bias errors within 3% and 10%, for  $\alpha$  and  $\mathcal{D}$ , respectively. Super-diffusion was observed in resting muscle, and to a greater degree post-exercise. Resting MVF was between 0.0067 and 0.0139 and increased between 2.2- and 4.7-fold post-exercise.

## Conclusions

This model captures super-diffusive molecular motions consistent with perfusion, using a parsimonious representation of the DWI signal, providing approximations of MVF comparable with histological estimates. This signal model demonstrates low parameter estimation errors and thus holds potential for a wide range of applications in skeletal muscle and elsewhere in the body.

**Keywords:** microvascular volume, hyperemia, anomalous diffusion, super-diffusion, intravoxel incoherent motion, fractional calculus

## Introduction

Adequate perfusion at rest and with increasing metabolic demand is essential for the preservation of muscle health and musculoskeletal function [1]. Impairment of the microvasculature secondary to disease [2, 3] and aging [4] may profoundly impair skeletal muscle metabolism and cause loss of muscle mass and strength. Robust and descriptive quantitative methods for mapping and quantifying perfusion non-invasively are important tools for research aimed at understanding the interplay between muscle perfusion, metabolism, and musculoskeletal function and identifying new therapeutic targets.

Skeletal muscle is a complex multiscale porous structure in terms of both cellular structure and vasculature [5, 6]. DWI has proven to be a useful approach for probing both the cellular and circulatory properties, with various signal models used to evaluate different aspects of this tissue [7]. Accordingly, development of robust approaches to quantify anatomical and functional characteristics of tissue microvasculature using DWI in vivo is an active area of research. Examples of such approaches include mapping of microvascular pool size [8], architecture [9], and function [10, 11]. These require acquisition protocols and analysis models that are capable of distinguishing between signal arising from the microvascular space and that arising from parenchyma; this is often accomplished using the implicit assumption that the blood pool exhibits Gaussian distributed motions, albeit with greater diffusivity compared with water in parenchyma.

Detailed invasive measurements of red blood cell motions in the microvascular system suggest non-Gaussian jump length distributions [12, 13]. The vascular system exhibits a space-filling fractal network of branching tubes with each branch diameter showing a power-law relationship to its source vessel [6]. Indeed, quantitative microCT measurements in skeletal muscle demonstrate broad distributions of microvascular blood vessel diameters skewed towards larger vessel diameters [5]. Furthermore, within individual capillary vessels between 2 and 5  $\mu\text{m}$  in diameter, the distribution of blood flow velocities span a tenfold range skewed towards larger velocities [12]. Given the superposition of these structural features of the microvasculature that would produce a broad distribution of blood flow velocities and broad range of blood flow velocities within capillaries, there might be limitations in modeling incoherent motions of the

microvascular blood pool using the assumption of a classical Gaussian distributed probability of jump lengths.

This work proposes an anomalous super-diffusion model, which is non-Gaussian diffusion exhibiting greater particle spread than that of the Gaussian case. This model extends Fick's first law through application of a space-fractional derivative instead of the classical integer-order derivative. The fractional-space derivative gives rise to a power-law relationship between mean squared displacement and time,  $\langle [x(t) - x(0)]^2 \rangle \propto t^{2/\alpha}$  and produces a stretched exponential signal decay as a function of  $b$ -value. The stretching parameter,  $\alpha$ , is connected to a stable distribution of particle jump lengths, which is a generalization of the Gaussian distribution. This approach provides a parsimonious representation of motional properties of skeletal muscle perfusion and can be interpreted in terms of skeletal muscle microvascular volume. Numerical simulations estimate model parameter errors under in vivo imaging conditions, and examine conditions of limited signal-to-noise and residual fat signal. Simulations also evaluate the effect of a reduced number of  $b$ -values, as would be required for increased temporal resolution in dynamic studies of perfusion changes, e.g. evaluating the time-course of post-exercise hyperemia.

## Theory

The following is adapted from work in the field of hydrology that develops a fractional advection-dispersion equation for describing transport of ground water contaminants in a heterogeneous aquifer [14, 15]. Molecular diffusion is modeled using the deterministic partial differential equation:

$$\frac{\partial c}{\partial t} = -\mathcal{D} \frac{\partial^2 c}{\partial x^2}, \quad (1)$$

which describes the concentration of molecules for a given location in a continuum. The solution to this equation in unrestricted diffusion describes a Gaussian concentration distribution with zero mean, and variance that is related to the macroscopic diffusion coefficient,  $\mathcal{D}$ .

Underlying the diffusion equation is Fick's first law:

$$F = -\mathcal{D} \frac{\partial C}{\partial x}, \quad (2)$$

which indicates that the flux,  $F$ , of molecules per unit area per unit time, is proportional to the spatial gradient of the concentration. It can be shown when deriving one-dimensional flux using a finite difference approach (see Appendix A.) that to recover Fick's first law, as the limit of the cell dimension approaches zero, molecular jump lengths  $\Delta x$  must be proportional to  $\Delta t^{1/2}$ . This relationship constrains molecular motions to a finite length scale per unit time.

For incoherent motions exhibiting broad distributions of jump lengths, as expected in the microvascular system, the constraint of molecular jumps to a particular length scale for a given time interval is removed through the incorporation of the fractional derivative into Fick's first law:

$$F = -\mathcal{D} D_{\beta}^m(C), \quad (3)$$

where  $D_{\beta}^m(C)$  is the fractional derivative of order  $m$  [16]. Fractional derivatives are frequently defined as a combination of left- (i.e. over the interval  $-\infty$  to  $x$ ) [17] and right-side (i.e. over the interval  $x$  to  $\infty$ ) [18] derivatives denoted as  $D_{\beta}^m$ , where  $\beta$  is the relative weighting of left- and right-side derivative functions. Unlike the integer-order equivalent, this fractional-order version of Fick's first law requires molecular jump lengths,  $\Delta x$ , to be proportional to  $\Delta t^{1/(m+1)}$ , where  $m$  is the order of the derivative, which could be rational or integer; this removes the scale dependence on molecular velocities allowing for jump lengths exhibiting greater spread than the Gaussian distribution at the tails.

Substituting fractional Fick's first law into the one-dimensional conservation of mass equation:

$$-\frac{\partial C}{\partial t} = \frac{\partial F}{\partial x}, \quad (4)$$

yields the space-fractional diffusion equation

$$\frac{\partial C}{\partial t} = \frac{\partial}{\partial x} \left( -\mathcal{D} D_{\beta}^m(C) \right) = -\mathcal{D} D_{\beta}^{\alpha}(C), \quad (5)$$

with an integer time derivative and where  $\alpha = m + 1$  and thus  $1 \leq \alpha \leq 2$ . See Appendix A. for additional details.

The stochastic (random walk) model can connect diffusion model parameters to a probability distribution of molecular motions within a continuum. For a large sum,  $n$ , of independent and identically distributed (*iid*) molecular jumps,  $\Delta x_i \mid i = (1, 2, \dots, n)$ , with finite variance, the central limit theorem states that an appropriately normalized sum of jumps converges to a Gaussian distribution ( $N$ ) with mean zero and unit variance:

$$\lim_{n \rightarrow \infty} \frac{\Delta x_1 + \Delta x_2 + \dots + \Delta x_n}{\sigma(n)^{\frac{1}{2}}} = Y \sim N(\mu = 0, \sigma^2 = 1), \quad (6)$$

forming a foundation for describing Brownian motion. The total number of jumps,  $n$ , can be replaced by the ratio of the total time,  $t$ , divided by the time increment  $\Delta t$ , (i.e.  $n = t/\Delta t$ ). This limit implies that the molecular displacement grows at the same rate as  $(t/\Delta t)^{1/2}$ .

The central limit theorem is a special case of the general limit (Levy) theorem which states that any *iid* random variable will converge to a stable distribution  $S_\alpha(\mu, \beta, \sigma)$ , yielding the following result for a random walk process:

$$\lim_{\frac{t}{\Delta t} \rightarrow \infty} \frac{\Delta x_1 + \Delta x_2 + \dots + \Delta x_{\frac{t}{\Delta t}}}{\sigma\left(\frac{t}{\Delta t}\right)^{\frac{1}{\alpha}}} = Y \sim S_\alpha(\mu = 0, \beta, \sigma = 1). \quad (7)$$

Stable distributions are parameterized based on the index of stability  $0 < \alpha \leq 2$ , shift parameter  $\mu$ , skewness parameter  $-1 \leq \beta \leq 1$ , and spread parameter  $\sigma$ , with  $\alpha$  and  $\beta$  being synonymous with fractional derivative  $D_\beta^\alpha$  parameters in Eq. 5. Note that the stable distribution is equivalent to the Gaussian for  $\alpha = 2$ . In contrast to the Gaussian probability, the limit above implies that molecular displacement grows at the same rate as  $(t/\Delta t)^{1/\alpha}$  and thus does not constrain molecular jump lengths to a fixed length scale for a given time increment.

The mean squared displacement can be related as:

$$\langle [x(t) - x(0)]^2 \rangle \propto t^{2/\alpha}, \quad (8)$$

and produces this super-diffusive ( $2/\alpha > 1$ ) behavior for  $\alpha < 2$  [19]. This can be appreciated in Figure 1, which shows a series of one dimensional random-walker jumps

for Gaussian (Fig. 1A) and non-Gaussian super-diffusion (Fig. 1B) conditions, with the latter showing large jump lengths.

## Methods

### Signal model

As described in Eq. 5, the diffusion equation can be expressed in terms of the space-fractional derivative:

$$\frac{\partial C(x, t)}{\partial t} = \mathcal{D}_{1, \alpha} \frac{\partial^\alpha C(x, t)}{\partial x^\alpha}, \quad (9)$$

where  $1 < \alpha \leq 2$  represents the order of the fractional derivative and is related to the jump length probability distribution as described in Eq. 7. Note  $\alpha$  in Eq. 9 is equivalent to the variable  $\beta$  previously described in the continuous time random walk model of Magin et al. [20-22]. For a displacement  $r = x(t) - x_0$ , the probability density of displacements  $P(r, t)$  has been shown to be equivalent to the solution to Eq. 9 [23]. It has previously been shown that the signal from the pulsed field gradient diffusion measurement is proportional to the Fourier transform (FT) of the averaged probability density of displacements [24]. Based on Eq. 9, the following expression has previously been derived [22]:

$$p(q, t) = \exp(-\mathcal{D}_{1, \alpha} |q|^\alpha t), \quad (10)$$

where  $p(q, t)$  is the FT in space of the displacement probability density  $P(r, t)$ , and  $\mathcal{D}_{1, \alpha}$  is the generalized diffusion coefficient with units  $\text{mm}^\alpha/\text{s}$ . Ingo et al. provide a compact form of this expression as a function of  $b$ -value, making the substitution  $b = q^2 t$ :

$$p(b) \propto S(b) = S(0) \cdot \exp\left(- (b\mathcal{D})^{\frac{\alpha}{2}}\right), \quad (11)$$

where  $S(b)$  is the diffusion signal intensity,  $S(0)$  is signal intensity at  $b=0$ ,  $\mathcal{D}$  is diffusivity scaled by a constant coefficient, with units  $\text{mm}^2/\text{s}$  and the exponent  $\alpha$  is equivalent to the fractional derivative order [22]. Therefore, the model parameter  $\mathcal{D}$  follows from

spread parameter  $\sigma$  [25], and  $\alpha$  is equivalent to the index of stability in the stable distribution, and thus reflects the likelihood of jump lengths.

### Numerical simulations

Numerical simulations were used to evaluate fit errors in the presence of residual unsuppressed fat signal and image noise, to examine the utility of this model for in vivo imaging. Diffusion-weighted signals were generated using the following stretched exponential function:

$$S(b) = S(0) \cdot \left( (1 - f_f) \cdot \exp\left(- (b\mathcal{D})^{\frac{\alpha}{2}}\right) + f_f \right) + \varepsilon_n, \quad (12)$$

where tissue parameter values ( $\mathcal{D}$  and  $\alpha$ ) were varied over a range of values observed in experimental data. Simulations did not account for anisotropic effects. An additional fat fraction ( $f_f$ ) term was included and varied from 0 to 18% in increments of 2%, to cover the range of residual fat signal magnitudes reported in healthy skeletal muscle [26, 27]. Modeling fat as a constant offset is a reasonable approximation for the relatively low  $b$ -values studied in this work, given that the reported ADC of fat is  $4 \times 10^{-5}$  mm<sup>2</sup>/s—two orders of magnitude smaller than diffusion in free water [26]. Simulated  $b$ -values were based on the current and previous experimental studies, respectively [11, 28, 29]: (1) 0, 3, 7, 10, 15, 20, 25, 30, 40, 50, 70, 100, 200, 400, 600, 800 s/mm<sup>2</sup>; and (2) 0, 10, 85, and 800 s/mm<sup>2</sup>. The first set is equivalent to our experimental acquisition, seeking to capture a maximum contribution from the microvasculature blood pool, and the second set represents a more limited acquisition, previously used to reduced scan time [30].

Synthetic signals were simulated for each set of tissue and acquisition parameters and Rician noise was added. This was achieved by adding zero-mean Gaussian noise to each channel of the complex decay signal to achieve a specified SNR defined by the ratio of the  $b=0$  signal to the standard deviation of the noise [31]. Each set of simulation parameters were generated using 1,000 independent noise realizations. Data simulated using Eq. 12 were fit to Eq. 11 and the same model with an offset term,  $B$ , to examine model fit performance when correcting for fat contamination:

$$S(b) = S(0) \cdot \exp\left(- (b\mathcal{D})^{\frac{\alpha}{2}}\right) + B, \quad (13)$$

using a Levenberg-Marquardt nonlinear least squares algorithm. Relative bias was defined as the mean parameter value over all noise realizations subtracted from the true input simulated parameter value normalized by the true input value:  $(\text{true}-\text{mean})/\text{true}$ . Dispersion was defined as the standard deviation of the fit parameter over all noise realizations divided by the true input simulation value.

### In vivo DWI measurements

Four healthy volunteers were recruited (28-72 years old) and enrolled. Ethical approval was obtained from the local Institutional Review Board and, in accordance with the Declaration of Helsinki, a full description of the study was provided, including any associated risks, and informed consent was obtained before any information was collected or procedure performed. Exclusion criteria included standard contraindications to MRI, frailty, severe cardiovascular disease and peripheral artery disease. Study participants were imaged using a 3T Achieva MRI scanner (Philips Healthcare, Best, Netherlands) before and after in-magnet exercise in one session.

In-magnet exercise was performed as previously described by our group [32]. Briefly, participants were positioned supine, feet first on the MRI table equipped with a customized MR-compatible ergometer (Quadspect, Ergospect, Innsbruck, Austria). Knees were supported at about 120° flexion with the ankles positioned under pedals designed for dynamic knee extension exercise. Study participants were instructed to use their quadriceps muscles to perform dynamic knee extension exercise by moving the pedal (up and down). After obtaining baseline DWI measurements of the thigh at rest, participants performed exercise using a frequency of 45 repetitions per minute for 2.5 minutes using the left leg. A fixed pedal resistance of 0.4 bar was used for all subjects.

Imaging was performed using a two-channel SENSE flexible coil positioned at the mid-thigh level, with one loop on the anterior aspect of the thigh and the other on the posterior aspect. Anatomic imaging included a 2D mDixon sequence with FOV 256 × 224 mm (voxel size 1 × 1 × 22 mm) to assist in region of interest (ROI) analysis. DWI was acquired using a single transverse slice at 60% of the total femur length above the medial epicondyle with a slice thickness of 22 mm, using a spin echo single-shot EPI

readout with diffusion sensitization in the slice direction. This sequence included a triple fat suppression approach that combines water-specific excitation, slice-select gradient reversal and spectral attenuated inversion recovery, to reduce the deleterious impact of fat signal on our measurements [27]. Imaging parameters included TR=3000 ms, TE=46 ms, SENSE factor 2, FOV 256 × 225 mm, matrix size 224 × 224; partial Fourier factor 0.6, and 16  $b$ -values (see  $b$ -value list (1) in Numerical simulations) as described in our previous work [32]. DWI data acquired prior to exercise at rest were obtained using NSA=20 (acquisition time 16.05 min) to provide an increased signal-to-noise ratio (SNR) under low perfusion conditions. Post-exercise DWI acquired dynamically after exercise was performed using NSA=4 (acquisition time 3.25 min) to permit finer temporal resolution during post-exercise hyperemia. The SNR for DWI was computed based on analysis of the  $b=0$  image and a noise-only image obtained using an identical sequence with radiofrequency and gradient pulses turned off, making appropriate corrections for Rician distributed noise [27, 31, 32].

ROIs were carefully defined using both diffusion and mDixon images (as a reference) in both agonist and antagonist muscle groups (Figure 2A) excluding macroscopic signs of fasciae, fat, and blood vessels. Fits to Eq. 11 were performed using the average signal intensity from each ROI for each  $b$ -value. Group averages for model fit parameters were reported as mean (SD) for each muscle group by averaging over all participants (Figure 2B).

Estimates of microvascular volume fraction (MVF) were computed based on experimental fit parameters. Fitted values of  $\mathcal{D}$  and  $\alpha$  were used to compute the cumulative distribution function (CDF) from the corresponding stable distribution. Using the experimental diffusion encoding time, the CDF was integrated over a range of jump lengths spanning observed red blood cell velocities in skeletal muscle capillaries [12] to estimate the relative signal fraction within the capillary vessels. These computed fractions were then adjusted for relaxation effects using the same procedure used in intravoxel incoherent motion analysis [27].

A pair-wise t-test was used to compare differences in fit parameter values and MVF estimates for each muscle group between baseline and post-exercise conditions. The F-test was used to evaluate if the stretching parameter resulted in a statistically

significant improvement in mean squared error [33]. All analysis and simulations were performed using MATLAB (The MathWorks, Natick, MA).

## Results

All experimental DWI data yielded  $\text{SNR} > 200$ . Under experimental imaging conditions (i.e. 16  $b$ -values with  $\text{SNR} = 200$ , black symbols), numerical simulation results based on fits using Eq. 11 demonstrate a positive bias in both  $\alpha$  and  $\mathcal{D}$  with increasing fat content (Figure 3A and 3C). In Figure 3B and D, both model parameters based on Eq. 11 show low dispersion in fit estimates within 1.5% and 1% for  $\alpha$  and  $\mathcal{D}$ , respectively. Bias and dispersion of parameter estimates showed no noticeable relationship with the underlying model input parameters under these simulation conditions. Blue symbols in Figure 3 shows simulation results based on fits using Eq. 13, demonstrating the expected trade-off in bias and dispersion that arises from including the offset fit parameter. Figure 3A and C based on Eq. 13 show a negative relative bias that is smaller compared with those of Eq. 11. All four panels suggest a moderate relationship between simulated fat fraction and bias and dispersion. Dispersion errors are slightly larger using Eq. 13 compared with those using Eq. 11, as would be expected from a model that incorporates an offset fit parameter in the presence of fat.

Black symbols in Figure 4 show simulation results based on fits using Eq. 11 under imaging conditions with a reduced number of  $b$ -values (4  $b$ -values) and lower SNR ( $\text{SNR} = 50$ ). Eq. 11 results in Figure 4A and C show almost identical relative bias in both model parameters as was observed under more favorable acquisition conditions in Figure 3. Figure 4B and D show elevated dispersion in  $\alpha$  and  $\mathcal{D}$  compared with Figure 3, as expected with fewer  $b$ -values and reduced SNR. Similar to results in Figure 3, input simulation parameters seem to have negligible influence on relative bias and dispersion in Figure 4 based on Eq. 11. Blue symbols in Figure 4 show simulation results using Eq. 13 with these more challenging acquisition conditions, and the influence of input simulation parameters on both relative bias and dispersion can be appreciated in both  $\alpha$  and  $\mathcal{D}$  when a baseline offset term is fit in conjunction with this model. Both parameters

are over-estimated regardless of the amount of fat, and these overestimates are greater for smaller values of  $\alpha$ . Therefore, at smaller values of  $\alpha$  (greater amount of perfusion), Eq. 13 will underestimate the perfusion more than at lower levels of perfusion. An inverse relationship between the true value of  $\alpha$  and dispersion is also evident, where lower levels of perfusion (i.e. larger values of  $\alpha$ ) will result in less dispersion.

Qualitatively, stretched exponential fits closely represent the data, particularly over low  $b$ -values that are heavily perfusion-weighted (Figure 2B); residuals were typically smaller than 1% of the total signal. The F-test quantitatively showed a significant improvement in the fit using the stretched exponential compared with the monoexponential model, with an average  $p$ -value from all subjects and ROIs of 0.017. Table 1 shows quantitative comparison of model parameters from selected ROIs between pre- and post-exercise conditions. Significant increases in  $\mathcal{D}$  are observed in all knee extensor groups involved in exercise while the knee flexor muscle showed no change. There was a significant decrease in  $\alpha$  with exercise in the vastus lateralis and vastus intermedius, consistent with an increase in microvascular blood volume and blood flow velocity. Figure 5 shows parameter maps pre- and post-exercise illustrating these parameter changes with hyperemia.

Figure 6A illustrates the direct connection between stretched exponential parameter  $\alpha$  and the stable distributions, where fit parameters can be used to estimate distributions of jump lengths. Figure 6B shows a representative comparison between two stable cumulative distribution functions derived from fit parameters in knee extensors pre- and post-exercise, showing an increased probability of larger jump lengths post-exercise.

Table 2 shows average values of MVF by muscle group before exercise, which range from 0.0067 to 0.0139. Immediately following in-magnet exercise, these volume fractions increase up to fourfold their resting values in knee extensor muscles, with the largest increase observed in the vastus intermedius. The rectus femoris showed a trend towards increasing MVF but this was not statistically significant ( $P=0.09$ ). The biceps femoris showed no change in MVF ( $P=0.52$ ), as expected in muscles that were uninvolved in exercise.

## Discussion

The connection between this stretched exponential signal model and the stable probability distribution provides intuition into multiscale structures like skeletal muscle and the vascular system exhibit multiple length scales related by power laws [6]. Stable probability distributions have been shown to provide good predictions of molecular motions in multiscale and heterogeneous structures [25, 34] and these parameters have demonstrated a connection with fractal dimensions [35, 36]. In addition to arguments based on observed power law structural relationships, even within a narrow range of capillary diameters, there exist broad distributions of blood flow velocity. For example, intravital microscopy studies of skeletal muscle and brain tissue in capillaries with diameters between 2-5  $\mu\text{m}$  showed a distribution of flow velocities of red blood cells spanning a tenfold range with a skew towards greater velocities [12]. Further, observations of blood flow regulation within the capillaries show wide fluctuations of flow velocity at rest in a single capillary over the span of minutes. Others have reported similar observations of broad distributions of blood flow velocities in vivo in capillaries and arterioles [12, 13, 37].

In the current work, the stretched exponential function fits multi- $b$ -value DWI data from low  $b$ -values, i.e.  $b \times D \leq 1$ . Super-diffusive features of the decay are most prominent in  $b$ -values less than  $\sim 250 \text{ s/mm}^2$ . These fits produce stretching parameter values less than 2 that reflect a probability of jump lengths greater than that predicted from Gaussian diffusion. The improvement of stretched exponential fits over the monoexponential model was demonstrated statistically using the F-test, which showed the addition of the stretching exponent significantly reduced fitting errors. Stretched exponential model parameters changed significantly due to exercise-induced hyperemia, reflecting an increase in super-diffusion attributed to the microvascular blood pool. The shape of the model decay curve consistently fit the data at rest and post-exercise, suggesting this parsimonious model is flexible enough to capture these dynamic changes in the decay shape. This is consistent with previous work applying this model in other tissues exhibiting large perfusion fractions like in the prostate [38].

To evaluate this model further, microvascular volume fractions were estimated based on stretched exponential fit parameters to compare with reported capillary

density measurements. As noted, the stretching parameter,  $\alpha$ , is equivalent to the stability index and  $\mathcal{D}$  can be related to the spread parameter [25] of the stable distribution allowing for probabilities to be calculated over a range of jump lengths (i.e. red blood cell velocities) observed in the capillary bed of skeletal muscle [12, 13, 37]. Based on typical reported densities of  $\sim 330$  capillaries per  $\text{mm}^2$  of tissue and an average capillary diameter of  $5 \mu\text{m}$ , a capillary volume fraction of 0.0065 can be estimated. Through integrating stable CDF's over the range of reported red blood cell velocities, MVF in the current study was estimated between 0.0067 and 0.0139 in resting skeletal muscle. This volume fraction increased between 2.2- and 4.7-fold during hyperemia, which is consistent with reported changes observed in skeletal muscle [39, 40].

The performance of the stretched exponential fits in the presence of noise and residual fat signal has been demonstrated previously and shown to produce more reliable estimates than other models such as the bi-exponential model [27, 33, 38]. For DWI applications in skeletal muscle perfusion, one important consideration that is not widely examined is the impact of fat signal on model parameter estimates [32]. This is particularly relevant in aging and musculoskeletal disease, which involve fatty replacement of muscle tissue and increased intramuscular and subcutaneous fat. Although fat suppression techniques reduce the contribution of fat signal, elimination of this signal is never completely realized so must be considered. Furthermore, chemical shift effects give rise to spatially-shifted fat signals in DWI sequences using single shot EPI readouts [27]. Simulations in the current work provide a simplified analysis of the impact of residual unsuppressed fat on the stretched exponential model both with and without an offset term and did not attempt to incorporate spectral modeling of fat. These analyses illustrate how, for low fractions of fat contamination, either model is reasonable, demonstrating relative low errors, but for larger fat signals the use of a baseline offset term will improve the interpretation of model parameters. Specifically, bias errors due to increased fat contamination would result in an underestimate of  $\alpha$ , which would be misinterpreted as greater perfusion; such a conclusion could be antithetical to the underlying physiology. This is an important consideration in conditions such as neuromuscular disease, which can result in substantial fat replacement.

An additional consideration for skeletal muscle perfusion studies is the need for higher temporal resolution to capture rapid perfusion dynamics, i.e. post-exercise hyperemia. The current work minimized acquisition time through limiting diffusion sensitization to the head-to-foot direction, approximately parallel to the thigh muscles, where maximum perfusion would be expected. Scan time is most readily reduced by minimizing the number of signal averages and  $b$ -values for a given dynamic, limiting the ability to obtain robust fits, and degrading SNR. However, simulations using only four  $b$ -values and modest SNR demonstrate robust parameter estimates with the stretched exponential model. For low residual fat fractions (less than 5%), bias errors are within 2.5% and 10% and dispersion within 9% and 8% for  $\alpha$  and  $\mathcal{D}$ , respectively (Figure 4). Under these restrictive conditions, incorporation of the additional baseline offset fitting parameter results in greater bias and dispersion results, which is expected given the limited number of  $b$ -values measured. The tradeoff between bias and dispersion errors in this low SNR and limited  $b$ -value situation shows the limitations of this model for absolute quantitation of perfusion, but its low dispersion suggests its strength for detecting dynamic changes in perfusion with reasonable precision (within  $\sim 10\%$ ).

Improved methods for in vivo characterization of skeletal muscle perfusion are of particular importance for evaluation of the overall function of skeletal muscle and how function is modulated in disease and aging, and with therapeutic interventions. DWI provides quantitative information on molecular motions of water and blood in tissue, making it appealing for in vivo measurements. Attempts to disentangle and quantify the properties of these different compartments have been the subject of numerous studies. Average resting  $\alpha$  values in the current study are within the wider range (i.e. 1.73 to 1.96) reported in a recent aging study of individuals 22-89 years old, which showed a positive association between  $\alpha$  and age [30]. The current work provides a physical model for more detailed interpretation of  $\alpha$  as it relates to microvascular properties. Although these analyses have been initially focused on a single diffusion direction, robust parameter estimates suggest feasibility of extending this model to a tensor form to allow for combined measures of anisotropic properties of microvascular perfusion and muscle fibers.

Although the current work was focused on skeletal muscle perfusion, several studies have used of stretched exponential DWI in other settings, particularly using large  $b$ -value acquisitions ( $b \times D > 1$ ) in the context of hindered diffusion. Early work by Bennet et al. reported the stretched exponent as a heterogeneity parameter representing the superposition of a distribution of diffusion coefficients [41]. Hall and Barrick elegantly demonstrated a connection between a fractal dimension and the stretching exponent showing examples of this analysis in healthy human brain [42]. Others have demonstrated utility of this model to probe tissue microstructure in the context of tumor imaging [43-45].

More recent work incorporating lower  $b$ -values ( $b \times D < 1$ ) where tissue perfusion would play more of a role, has demonstrated the ability to distinguish high grade glioblastoma [46] and shown efficacy in staging liver fibrosis [47] and detection of prostate cancer [38]. Mazaheri et al. proposed the stretched exponential model as a more robust, heuristic alternative to the intravoxel incoherent motion model to quantify perfusion, noting lower bias and dispersion errors. These examples demonstrate an increasing application of the stretched exponential model incorporating low  $b$ -value measurements in other tissues in which quantitative measures of perfusion are important.

## Conclusion

A fractional Fickian diffusion model provides an intuitive picture for interpreting non-Gaussian super-diffusion in a continuum, connecting parameters from the stretched exponential signal model to a stable probability distribution of jump lengths. This signal model captures perfusion motions with the parsimonious representation of a stretched exponential. Analysis of skeletal muscle DWI at rest and during hyperemia provides close approximations of microvascular volumes comparable with histological estimates. This signal model demonstrates low estimation errors that are predictable and thus holds potential for a wide range of applications.

## **Acknowledgments**

This research was supported in part by the Intramural Research Program of the NIH, National Institute on Aging.

## References

1. Poole, D.C., *Edward F. Adolph Distinguished Lecture. Contemporary model of muscle microcirculation: gateway to function and dysfunction*. J Appl Physiol (1985), 2019. **127**(4): p. 1012-1033.
2. Padilla, D.J., et al., *Effects of Type II diabetes on capillary hemodynamics in skeletal muscle*. Am J Physiol Heart Circ Physiol, 2006. **291**(5): p. H2439-44.
3. Bradley, J.R., et al., *Impaired nutritive skeletal muscle blood flow in patients with chronic renal failure*. Clin Sci (Lond), 1990. **79**(3): p. 239-45.
4. Socha, M.J. and S.S. Segal, *Microvascular mechanisms limiting skeletal muscle blood flow with advancing age*. J Appl Physiol (1985), 2018. **125**(6): p. 1851-1859.
5. Laura, S., et al., *Correlative Imaging of the Murine Hind Limb Vasculature and Muscle Tissue by MicroCT and Light Microscopy*. Scientific Reports, 2017. **7**(1).
6. West, G.B., J.H. Brown, and B.J. Enquist, *A general model for the origin allometric scaling laws in biology*. Science, 1997. **276**(5309).
7. Lima, M. and D. Le Bihan, *Clinical Intravoxel Incoherent Motion and Diffusion MR Imaging: Past, Present, and Future*. Radiology, 2016. **278**(1): p. 13.
8. Le Bihan, D., et al., *Separation of diffusion and perfusion in intravoxel incoherent motion MR imaging*. Radiology, 1988. **168**(2): p. 497-505.
9. Karampinos, D.C., et al., *Intravoxel partially coherent motion technique: characterization of the anisotropy of skeletal muscle microvasculature*. J Magn Reson Imaging, 2010. **31**(4): p. 942-53.
10. Filli, L., et al., *Dynamic intravoxel incoherent motion imaging of skeletal muscle at rest and after exercise*. NMR Biomed, 2015. **28**(2): p. 240-6.
11. Nguyen, A., et al., *Application of intravoxel incoherent motion perfusion imaging to shoulder muscles after a lift-off test of varying duration*. NMR Biomed, 2016. **29**(1): p. 66-73.
12. Ivanov, K.P., M.K. Kalinina, and I. Levkovich Yu, *Blood flow velocity in capillaries of brain and muscles and its physiological significance*. Microvasc Res, 1981. **22**(2): p. 143-55.
13. Rosenblum, I.W., *Erythrocyte Velocity and a Velocity Pulse in Minute Blood Vessels on the Surface of the Mouse Brain*. Circulation Research, 1969. **24**(6): p. 887-892.
14. Schumer, R., et al., *Eulerian derivation of the fractional advection– dispersion equation*. Journal of Contaminant Hydrology, 2001. **48**(1-2): p. 69-88.
15. Schumer, R., M.M. Meerschaert, and B. Baeumer, *Fractional advection– dispersion equations for modeling transport at the Earth surface*. Journal of Geophysical Research: Earth Surface, 2009. **114**(F4): p. n/a-n/a.
16. Gorenflo, R. and F. Mainardi, *Fractional calculus and stable probability distributions*. Archives of Mechanics, 1998. **50**(3): p. 377-388.
17. Gorenflo, R. and F. Mainardi, *Random walk models for space-fractional diffusion processes*. Fractional Calculus Applied Analysis, 1998. **1**: p. 167-191.
18. Miller, K.S., *An introduction to the fractional calculus and fractional differential equations*, ed. B. Ross. 1993, New York: New York : Wiley.

19. Metzler, R. and J. Klafter, *The random walk's guide to anomalous diffusion: a fractional dynamics approach*. Physics Reports-Review Section of Physics Letters, 2000. **339**(1): p. 1-77.
20. Magin, R.L., et al., *Anomalous diffusion expressed through fractional order differential operators in the Bloch-Torrey equation*. J Magn Reson, 2008. **190**(2): p. 255-70.
21. Ingo, C., et al., *On random walks and entropy in diffusion-weighted magnetic resonance imaging studies of neural tissue*. Magn Reson Med, 2014. **71**(2): p. 617-27.
22. Ingo, C., et al., *Parsimonious continuous time random walk models and kurtosis for diffusion in magnetic resonance of biological tissue*. Front Phys, 2015. **3**.
23. McCall, D.W., D.C. Douglass, and E.W. Anderson, *Self- Diffusion Studies by Means of Nuclear Magnetic Resonance Spin- Echo Techniques*. Berichte der Bunsengesellschaft für physikalische Chemie, 1963. **67**(3): p. 336-340.
24. Stejskal, E.O., *Use of Spin Echoes in a Pulsed Magnetic- Field Gradient to Study Anisotropic, Restricted Diffusion and Flow*. The Journal of Chemical Physics, 1965. **43**(10): p. 3597-3603.
25. Benson, D., et al., *Fractional Dispersion, Lévy Motion, and the MADE Tracer Tests*. Transport in Porous Media, 2001. **42**(1): p. 211-240.
26. Steidle, G., F. Eibofner, and F. Schick, *Quantitative diffusion imaging of adipose tissue in the human lower leg at 1.5 T*. Magn Reson Med, 2011. **65**(4): p. 1118-24.
27. Cameron, D., et al., *The effect of noise and lipid signals on determination of Gaussian and non-Gaussian diffusion parameters in skeletal muscle*. NMR Biomed, 2017. **30**(7).
28. Mastropietro, A., et al., *Triggered intravoxel incoherent motion MRI for the assessment of calf muscle perfusion during isometric intermittent exercise*. NMR Biomed, 2018: p. e3922.
29. Hiepe, P., et al., *Interrelations of muscle functional MRI, diffusion-weighted MRI and (31) P-MRS in exercised lower back muscles*. NMR Biomed, 2014. **27**(8): p. 958-70.
30. Adelnia, F., et al., *The Role of Muscle Perfusion in the Age-Associated Decline of Mitochondrial Function in Healthy Individuals*. Front Physiol, 2019. **10**: p. 427.
31. Sijbers, J., et al., *Estimation of the noise in magnitude MR images*. Magn Reson Imaging, 1998. **16**(1): p. 87-90.
32. Adelnia, F., et al., *Diffusion-weighted MRI with intravoxel incoherent motion modeling for assessment of muscle perfusion in the thigh during post-exercise hyperemia in younger and older adults*. NMR Biomed, 2019. **32**(5): p. e4072.
33. Reiter, D.A., et al., *Anomalous T2 relaxation in normal and degraded cartilage*. Magn Reson Med, 2016. **76**(3): p. 953-62.
34. Benson, D.A., S.W. Wheatcraft, and M.M. Meerschaert, *The fractional- order governing equation of Lévy Motion*. Water Resources Research, 2000. **36**(6): p. 1413-1423.
35. Makse, H., J. Andrade, and H. Stanley, *Tracer Dispersion in Porous Media with Spatial Correlations*. arXiv.org, 1998.

36. Capuani, S. and M. Palombo, *Mini Review on Anomalous Diffusion by MRI: Potential Advantages, Pitfalls, Limitations, Nomenclature, and Correct Interpretation of Literature*. *Frontiers in Physics*, 2020. **7**(248).
37. Ma, Y.P., et al., *On- line measurement of the dynamic velocity of erythrocytes in the cerebral microvessels in the rat*. *Microvascular Research*, 1974. **8**(1): p. 1-13.
38. Mazaheri, B.Y., et al., *Diffusion- Weighted Magnetic Resonance Imaging of the Prostate: Improved Robustness With Stretched Exponential Modeling*. *Journal of Computer Assisted Tomography*, 2012. **36**(6): p. 695-703.
39. Honig, C.R., C.L. Odoroff, and J.L. Frierson, *Capillary recruitment in exercise: Rate, extent, uniformity, and relation to blood flow*. *American Journal of Physiology - Heart and Circulatory Physiology*, 1980. **7**(1): p. H31-H42.
40. Johnson, P.C., et al., *Effect of occlusion duration on reactive hyperemia in sartorius muscle capillaries*. *The American journal of physiology*, 1976. **230**(3): p. 715.
41. Bennett, K.M., et al., *Characterization of continuously distributed cortical water diffusion rates with a stretched-exponential model*. *Magnetic Resonance in Medicine*, 2003. **50**(4): p. 727-734.
42. Hall, M.G. and T.R. Barrick, *From diffusion- weighted MRI to anomalous diffusion imaging*. *Magnetic Resonance in Medicine*, 2008. **59**(3): p. 447-455.
43. Hoff, B.A., et al., *Assessment of multiexponential diffusion features as MRI cancer therapy response metrics*. *Magnetic Resonance in Medicine*, 2010. **64**(5): p. 1499-1509.
44. Liu, C., et al., *Breast lesion characterization using whole- lesion histogram analysis with stretched- exponential diffusion model*. *Journal of Magnetic Resonance Imaging*, 2018. **47**(6): p. 1701-1710.
45. Xu, J., et al., *A comparative assessment of preclinical chemotherapeutic response of tumors using quantitative non-Gaussian diffusion MRI*. *Magnetic Resonance Imaging*, 2017. **37**: p. 195-202.
46. M., K., et al., *Differentiation of high- grade from low- grade diffuse gliomas using diffusion- weighted imaging: a comparative study of mono-, bi-, and stretched- exponential diffusion models*. *Neuroradiology*, 2020. **62**(7): p. 815-823.
47. Seo, N., et al., *Liver fibrosis: stretched exponential model outperforms mono- exponential and bi- exponential models of diffusion- weighted MRI*. *European Radiology*, 2018. **28**(7): p. 2812-2822.
48. Podlubny, I., *Fractional differential equations an introduction to fractional derivatives, fractional differential equations, to methods of their solution and some of their applications*. 1999, San Diego: San Diego : Academic Press.
49. Osler, T.J., *Taylor's Series Generalized for Fractional Derivatives and Applications*. *SIAM Journal on Mathematical Analysis*, 1971. **2**(1): p. 37-48.

**Table 1.** Region of interest analysis of stretched exponential model parameters from healthy volunteers before and immediately after in-magnet exercise. Changes in  $\mathcal{D}$  and  $\alpha$  reflect post-exercise hyperemia in knee extensor muscles used during exercise. Symbols reflect levels of significance between pre- (resting) and post-exercise (hyperemia) conditions with <sup>(a)</sup>  $p < .05$ , <sup>(b)</sup>  $p = .01$ , <sup>(c)</sup>  $p < .01$ , <sup>(d)</sup>  $p < .005$ , <sup>(e)</sup>  $p < .001$ .

Muscle group	Resting		Hyperemia	
	$\mathcal{D}$ $\mu\text{m}^2/\text{ms}$	$\alpha$	$\mathcal{D}$ $\mu\text{m}^2/\text{ms}$	$\alpha$
Rectus femoris (green)	2.1 (0.2)	1.88 (0.07)	2.6 (0.1) <sup>(a)</sup>	1.83 (0.04)
Vastus lateralis (blue)	2.3 (0.2)	1.86 (0.09)	2.8 (0.2) <sup>(d)</sup>	1.59 (0.05) <sup>(b)</sup>
Vastus intermedius (red)	2.3 (0.1)	1.80 (0.05)	2.8 (0.1) <sup>(e)</sup>	1.56 (0.06) <sup>(c)</sup>
Biceps femoris (orange)	1.9 (.04)	1.86 (0.07)	1.9 (0.1)	1.81 (0.08)

**Table 2.** Microvascular fraction (MVF) estimates derived from analysis of stable cumulative distributions using fitted stretched exponential model parameters (Table 1). Integration of the cumulative distribution was performed over the range of reported capillary blood flow velocities. Pre- and post-exercise volumes are consistent with histological volume fractions. Symbol reflects significance between pre- and post-exercise conditions with <sup>(a)</sup>  $p < .01$ .

<b>Muscle group</b>	<b>MVF Resting</b>	<b>MVF Hyperemia</b>
Rectus femoris (green)	.0067 (.0049)	.0149 (.0050)
Vastus lateralis (blue)	.0099 (.0079)	.0463 (.0111) <sup>(a)</sup>
Vastus intermedius (red)	.0139 (.0057)	.0497 (.0099) <sup>(a)</sup>
Biceps femoris (orange)	.0069 (.0037)	.0102 (.0061)

## Figure Legends

**Figure 1.** One dimensional random walk simulation: A) Gaussian particle jumps with  $\alpha = 2$  reflecting the condition  $2/\alpha = 1$ . B) Non-Gaussian particle jumps with  $\alpha = 1.5$  reflecting the super-diffusion condition  $2/\alpha > 1$ . Simulations performed using codes provided in M.M. Meerschaert and A. Sikorskii *Stochastic Models for Fractional Calculus*, De Gruyter, 2012.

**Figure 2.** A) Representative region of interest selection from rectus femoris (RF, green), vastus lateralis (VL, blue), vastus intermedius (VI, red), and biceps femoris (BF, orange). B) Representative diffusion signal decay (open circles) from the VL at rest with stretched exponential model fit (dashed blue line) with fit residual (dot-dashed black line) below. An expanded semi-log view of the fit residual in the pane directly below the fit shows a magnified view of the fit error with values on the order of 0.1% of the total signal. The stretched exponential model fits data closely over the entire span of measured  $b$ -values.

**Figure 3.** A) Relative bias and B) dispersion in  $\alpha$  as a function of fat fraction. C) Relative bias and D) dispersion in  $\mathcal{D}$  as a function of fat fraction. All simulations based on 16  $b$ -values and SNR=200. Figure symbols represent:  $\circ$  input  $\alpha = 1.8$ ,  $*$  input  $\alpha = 1.7$ ,  $+$  input  $\alpha = 1.6$ . Black symbols reflect fits performed using Eq. 11, which does not use a baseline correction parameter. Blue symbols reflect fits performed using Eq. 13, which does use a baseline correction parameter.

**Figure 4.** A) Relative bias and B) dispersion in  $\alpha$  as a function of fat fraction. C) Relative bias and D) dispersion in  $\mathcal{D}$  as a function of fat fraction. All simulations based on 4  $b$ -values and SNR=50. Figure symbols represent:  $\circ$  input  $\alpha = 1.8$ ,  $*$  input  $\alpha = 1.7$ ,  $+$  input  $\alpha = 1.6$ . Black symbols reflect fits performed using Eq. 11, which does not use a baseline correction parameter. Blue symbols reflect fits performed using Eq. 13, which does use a baseline correction parameter.

**Figure 5.** Representative stretched exponential parameter maps  $\alpha$ ,  $\mathcal{D}$ , and microvascular volume fraction (MVF) at rest (top row) and during post-exercise

hyperemia (bottom row). Both  $\alpha$  and  $\mathcal{D}$  maps in the bottom row reflect the increased perfusion in knee extensor muscles due to hyperemia.

**Figure 6.** A) Representative displacement probability distributions based on the fractional Fickian model, plotted using stability index,  $\alpha$ , varied from 1.5 to 2 and all other parameters held constant. As  $\alpha$  decreases from a value of 2 the PDF exhibits heavy tails representing an increase in the probability of greater jump lengths. B) Representative displacement cumulative distributions showing the heavy tails with decreasing values of stability index,  $\alpha$ . Displacements correspond to typical diffusion coefficients observed and diffusion times used in the current study.

**Figure A.1.** A) Diagram illustrating random molecular jumps between adjacent cells in one-dimension with cell indices  $i$  and  $i+1$ , and finite length  $\Delta x$ . B) Diagram illustrating random particle jumps that occur in fractional Fickian diffusion, where molecular jumps are not constrained to adjacent cells.

## Figures

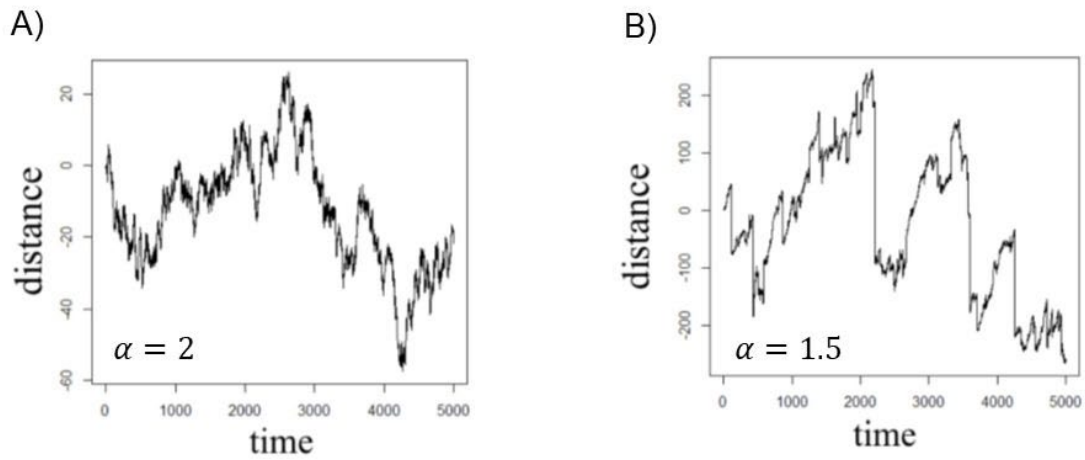


**Figure 1.** One dimensional random walk simulation: A) Gaussian particle jumps with  $\alpha = 2$  reflecting the condition  $2/\alpha = 1$ . B) Non-Gaussian particle jumps with  $\alpha = 1.5$  reflecting the super-diffusion condition  $2/\alpha > 1$ . Simulations performed using codes provided in M.M. Meerschaert and A. Sikorskii *Stochastic Models for Fractional Calculus*, De Gruyter, 2012.

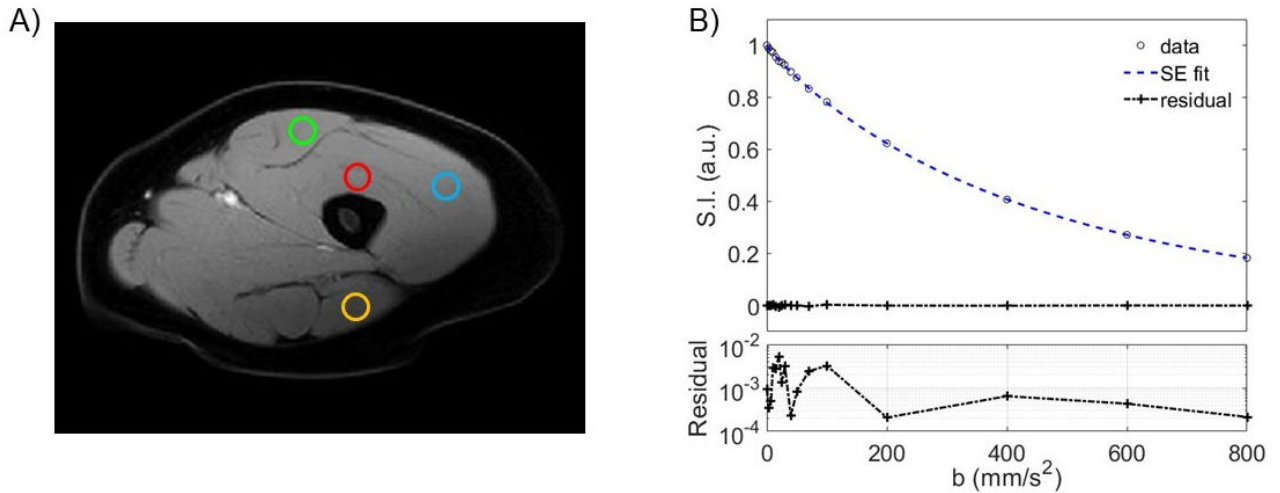


**Figure 2.** A) Representative region of interest selection from rectus femoris (RF, green), vastus lateralis (VL, blue), vastus intermedius (VI, red), and biceps femoris (BF, orange). B) Representative diffusion signal decay (open circles) from the VL at rest with stretched exponential model fit (dashed blue line) with fit residual (dot-dashed black line) below. An expanded semi-log view of the fit residual in the pane directly below the fit shows a magnified view of the fit error with values on the order of 0.1% of the total signal. The stretched exponential model fits data closely over the entire span of measured  $b$ -values.

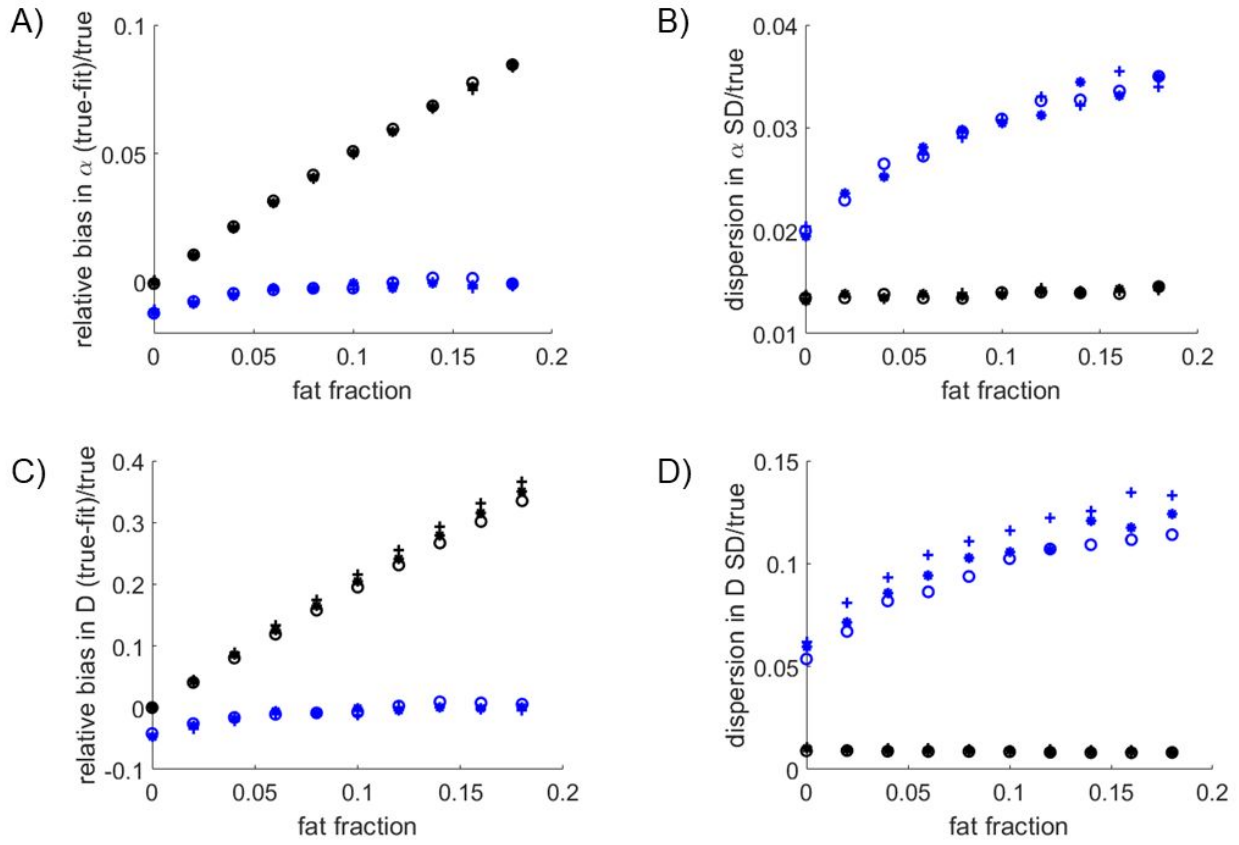


**Figure 3.** A) Relative bias and B) dispersion in  $\alpha$  as a function of fat fraction. C) Relative bias and D) dispersion in  $D$  as a function of fat fraction. All simulations based on 16  $b$ -values and SNR=200. Figure symbols represent:  $\circ$  input  $\alpha=1.8$ ,  $*$  input  $\alpha=1.7$ ,  $+$  input  $\alpha=1.6$ . Black symbols reflect fits performed using Eq. 11, which does not use a baseline correction parameter. Blue symbols reflect fits performed using Eq. 13, which does use a baseline correction parameter.

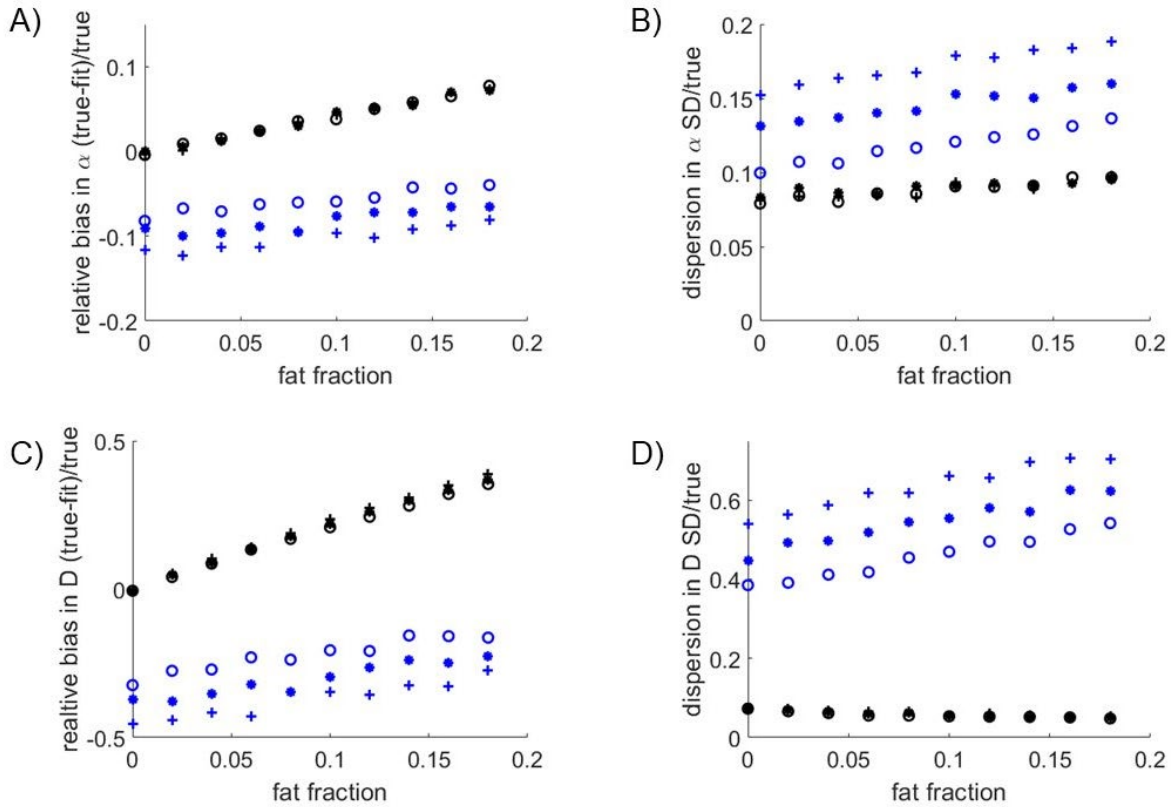


**Figure 4.** A) Relative bias and B) dispersion in  $\alpha$  as a function of fat fraction. C) Relative bias and D) dispersion in  $D$  as a function of fat fraction. All simulations based on 4  $b$ -values and SNR=50. Figure symbols represent:  $\bullet$  input  $\alpha = 1.8$ ,  $*$  input  $\alpha = 1.7$ ,  $+$  input  $\alpha = 1.6$ . Black symbols reflect fits performed using Eq. 11, which does not use a baseline correction parameter. Blue symbols reflect fits performed using Eq. 13, which does use a baseline correction parameter.

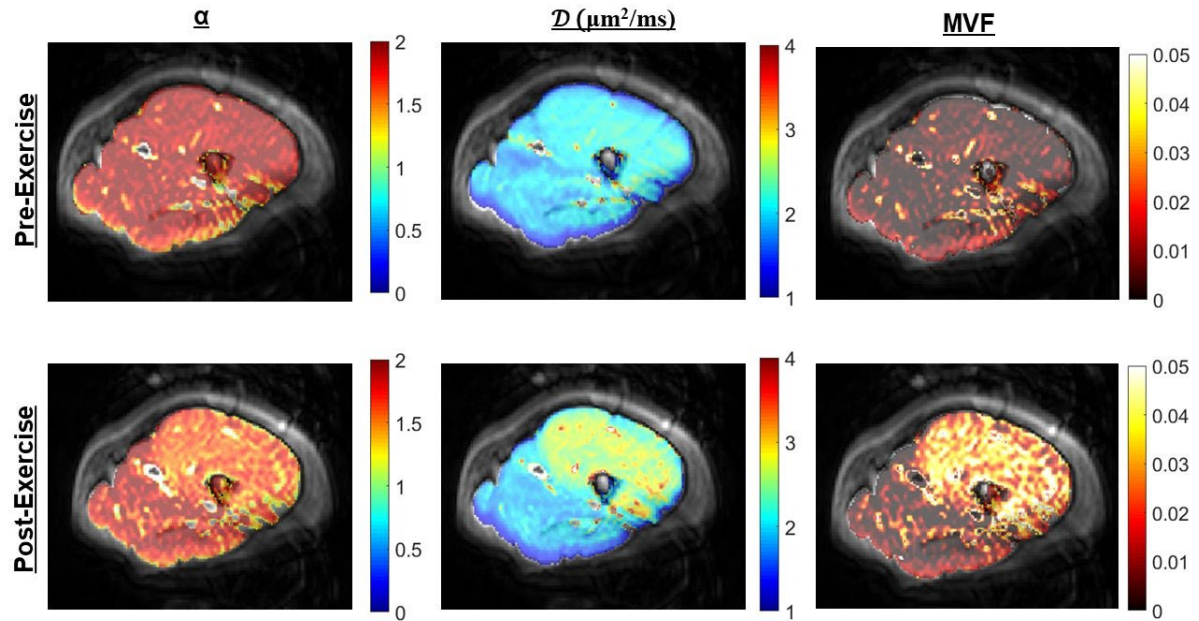


**Figure 5.** Representative stretched exponential parameter maps  $\alpha$ ,  $\mathcal{D}$ , and microvascular volume fraction (MVF) at rest (top row) and during post-exercise hyperemia (bottom row). Both  $\alpha$  and  $\mathcal{D}$  maps in the bottom row reflect the increased perfusion in knee extensor muscles due to hyperemia.

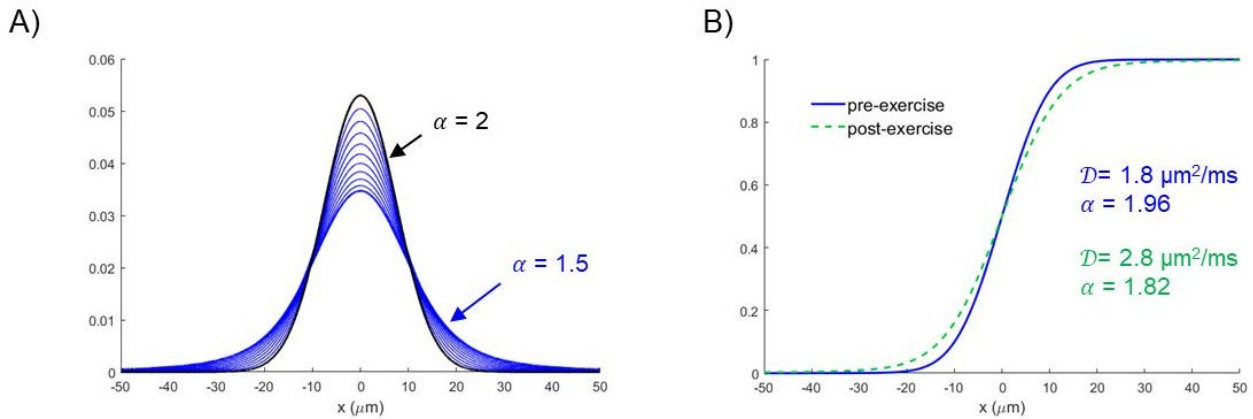


**Figure 6.** A) Representative displacement probability distributions based on the fractional Fickian model, plotted using stability index,  $\alpha$ , varied from 1.5 to 2 and all other parameters held constant. As  $\alpha$  decreases from a value of 2 the PDF exhibits heavy tails representing an increase in the probability of greater jump lengths. B) Representative displacement cumulative distributions showing the heavy tails with decreasing values of stability index,  $\alpha$ . Displacements correspond to typical diffusion coefficients observed and diffusion times used in the current study.

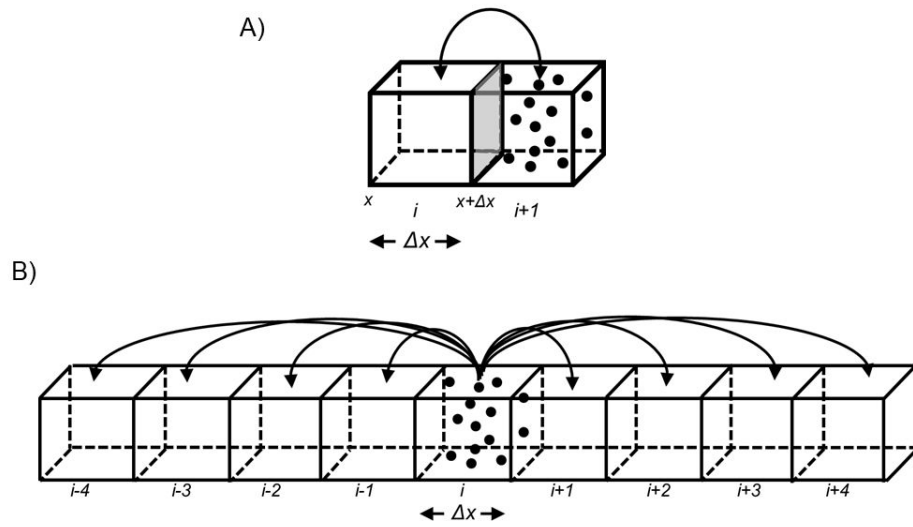


**Figure A.1.** A) Diagram illustrating random molecular jumps between adjacent cells in one-dimension with cell indices  $i$  and  $i+1$ , and finite length  $\Delta x$ . B) Diagram illustrating random particle jumps that occur in fractional Fickian diffusion, where molecular jumps are not constrained to adjacent cells.

## Appendix A

The following is an adaptation of detailed work by Schumer et al. describing the fractional advection dispersion equation both in the Eulerian [14] and Lagrangian [15] reference frame.

Fick's law relates the flux  $F$  of molecules to the molecular concentration  $C$  as:

$$F = -\mathcal{D}\nabla C(x, t), \quad \text{A.1}$$

where  $\mathcal{D}$  is the diffusion coefficient. For a one-dimensional molecular flux (Figure A.1.A), molecular concentration of the  $i^{\text{th}}$  cell, with volume  $\Delta v$ , containing  $N_i$  number of molecules, is expressed as  $C_i = \frac{N_i}{\Delta v}$ . For random molecular jumps occurring backwards and forwards to adjacent elements at a rate  $R$  in time interval  $\Delta t$ , the flux in the  $i^{\text{th}}$  element is expressed as:

$$F_i = \frac{1}{2}(C_i - C_{i+1})R\Delta x. \quad \text{A.2}$$

$C_{i+1} - C_i$  is equivalently written as  $C(x + \Delta x, t) - C(x, t)$  with Taylor series approximation:

$$\frac{\partial C}{\partial x}(x, t)\Delta x + \sigma(\Delta x). \quad \text{A.3}$$

Combining A.2 and A.3, flux becomes:

$$F_i = \frac{1}{2}\left(\frac{\partial C}{\partial x}\Delta x + \sigma(\Delta x)\right)R\Delta x. \quad \text{A.4}$$

To recover Fick's law (A.1) from Eq. A4 in the limit of  $\Delta x \rightarrow 0$ ,  $\frac{1}{2}\Delta x^2 R \rightarrow \mathcal{D}$  and  $\frac{1}{2}R\sigma(\Delta x^2) \rightarrow 0$ . This implies that  $\Delta x^2$  must decrease at the same rate that  $R$  increases, meaning  $\Delta x$  increases as  $(\Delta t)^{1/2}$ .

Non-local effects (Figure A.1.B) can be incorporated into Fick's law through the use of fractional derivatives, which are non-local functions that depend on the weighted average of values over the entire function [17, 18]. These weights correspond to a power function defined by the order of the fractional derivative [48].

Using the generalized Taylor series expansion [49], flux can be written in terms of the fractional derivative; thus,  $C(x + \Delta x, t) - C(x, t)$  becomes:

$$C(x + \Delta x, t) = \sum_{n=-\infty}^{\infty} D_{\beta}^{n+m}(C) \frac{\Delta x^{n+m}}{\Gamma(n+m+1)}, \quad \text{A.5}$$

$D_{\beta}^{n+m}$  is the fractional derivative with order  $n+m$ , where  $n$  is an integer index of summation,  $m$  is a rational number,  $\beta$  is a constant that weights the relative contribution of the left- and right-sided derivative, and  $\Gamma$  is the gamma function [17]. Detailed description of fractional derivatives can be found here [48]. Flux is written:

$$F = \frac{1}{2} \left( D_{\beta}^m(C) \frac{\Delta x^m}{\Gamma(m+1)} + \sigma(\Delta x^m) \right) R \Delta x, \quad \text{A.6}$$

and fractional Fick's law is recovered in the limit of  $\Delta x \rightarrow 0$

$$F = -\mathcal{D} D_{\beta}^m(C). \quad \text{A.7}$$

This implies that in the limit,  $\Delta x^m$  must decrease at the same rate that  $R$  increases, meaning  $\Delta x$  increases as  $(\Delta t)^{1/\alpha}$ , where  $\alpha = m + 1$ . Thus, molecules can move any distance from its origin in a given  $\Delta t$  with a probability that decays as a power-law defined by the order of the fractional derivative.